The Astrophysical Journal Letters, 921:L28 (6pp), 2021 November 10 https://doi.org/10.3847/2041-8213/ac2f3a

Detectable Abundance of Cyanoacetylene (HC_3N) Predicted on Reduced Nitrogen-rich Super-Earth Atmospheres

Paul B. Rimmer[1,2,3], Liton Majumdar[4], Akshay Priyadarshi[5], Sam Wright[6], and S. N. Yurchenko[6]
[1] Department of Earth Sciences, University of Cambridge, Downing Street, Cambridge CB2 3EQ, UK; pbr27@cam.ac.uk
[2] Cavendish Laboratory, University of Cambridge, JJ Thomson Avenue, Cambridge CB3 0HE, UK
[3] MRC Laboratory of Molecular Biology, Francis Crick Avenue, Cambridge CB2 0QH, UK
[4] School of Earth and Planetary Sciences, National Institute of Science Education and Research, HBNI, Jatni 752050, Odisha, India
[5] School of Physical Sciences, National Institute of Science Education and Research, HBNI, Jatni 752050, Odisha, India
[6] Department of Physics and Astronomy, University College London, Gower Street, London WC1E 6BT, UK
Received 2021 July 27; revised 2021 October 8; accepted 2021 October 11; published 2021 November 4

Abstract

We predict that cyanoacetylene (HC_3N) is produced photochemically in the atmosphere of GJ 1132 b in abundances detectable by the James Webb Space Telescope (JWST), assuming that the atmosphere is hydrogen dominated and rich in molecular nitrogen (N_2), methane (CH_4), and hydrogen cyanide (HCN), as described by Swain et al. First, we construct line lists and cross sections for HC_3N. Then we apply these cross sections and the model atmosphere of Swain et al. to a radiative transfer model in order to simulate the transmission spectrum of GJ 1132 b as it would be seen by JWST, accounting for the uncertainty in the retrieved abundances. We predict that cyanoacetylene features at various wavelengths, with a clear lone feature at 4.5 μm, observable by JWST after one transit. This feature persists within the 1σ uncertainty of the retrieved abundances of HCN and CH_4. The signal is detectable for stratospheric temperatures $\lesssim$600 K and moderate stratospheric mixing (10^6 cm^2 s^{-1} $\lesssim K_{zz} \lesssim 10^8$ cm^2 s^{-1}). Our results also indicate that HC_3N is an important source of opacity that future retrieval models should consider.

Unified Astronomy Thesaurus concepts: Extrasolar rocky planets (511); Exoplanet atmospheres (487)

1. Introduction

Cyanoacetylene (HC_3N) is a linear molecule composed of two triple-bonded carbons bound at one end with a hydrogen atom and at the other with a nitrile group: carbon and nitrogen joined by a triple bond: H–C ≡ C–C ≡ N. Because of its two energetic bonds, it is both physically stable and highly reactive in aqueous media (Ferris et al. 1968). It acts as both a molecular backbone and a source of chemical energy for prebiotic chemical synthesis (Powner et al. 2009; Becker et al. 2019). It can be produced from radical reactions between the cyano radical and acetylene and is a major product of the Miller–Urey synthesis (Miller 1953; Sanchez et al. 1966). There is extensive discussion among prebiotic chemists about whether HC_3N is prebiotically plausible (Orgel 2002).

HC_3N has been observed in the atmosphere of Titan from the ground, both in the gas phase (Bézard et al. 1992), and condensed into crystalline aerosol (Khanna 2005). According to retrieval from Atacama Large Millimeter/submillimeter Array (ALMA) observations, the abundance of HC_3N in the atmosphere of Titan is at about 100 ppb at 0.1–1 mbar, and drops by orders of magnitude with increasing pressure (Thelen et al. 2019).

Experimentally, the IR intensities of HC_3N were studied in Bénilan et al. (2006) and Douin et al. (2015). High-resolution spectroscopic analyses were reported by Bizzocchi et al. (2017) and Jiang et al. (2021).

Swain et al. (2021) analyze Hubble data of GJ 1132 b transmission spectra and find 0.5% concentrations of both hydrogen cyanide (HCN) and methane (CH_4) in an atmosphere with low mean molecular mass, implying the atmosphere is hydrogen dominated. Swain et al. (2021) report that the atmosphere may be volcanic, and their photochemical models predict significant amounts of HC_3N in the upper atmosphere. The analysis of Swain et al. (2021) has been challenged by Mugnai et al. (2021) and Libby-Roberts et al. (2021), who find no evidence of molecular features in the Hubble data. The analysis of Swain et al. (2021) and the response by Mugnai et al. (2021) and Libby-Roberts et al. (2021) are the latest in elaborate and conflicting literature attempting to determine the presence and nature of an atmosphere of GJ 1132 b (e.g., Schaefer et al. 2016; Southworth et al. 2017; Diamond-Lowe et al. 2018).

Regardless of whether GJ 1132 b has a reduced atmosphere, there is theoretical support for the persistence of volcanically derived, highly reduced atmospheres on rocky exoplanets, owing to the persistence of elemental iron in the mantle (Lichtenberg 2021). It is possible that many super-Earth atmospheres resemble a warm Titan composition.

For this Letter, we assume that the atmosphere reported by Swain et al. (2021) is the atmosphere of GJ 1132 b. Based on this assumption, we predict that HC_3N is present in the upper atmosphere of GJ 1132 b in abundances detectable by the James Webb Space Telescope (JWST), and is an indication of a reduced atmosphere with a significant fraction of chemically active nitrogen and carbon species. In Section 2, we describe the method for constructing a line list of HC_3N and the radiative transfer model, and the synthetic JWST pipeline used to calculate the transmission spectra. We present our results in Section 3, and discuss the promise and challenges for observing HC_3N on GJ 1132 b, and the application of this work beyond GJ 1132 b, in Section 4.

2. Methods

In order to make predictions about HC_3N in the atmosphere of GJ 1132 b, we first predict the atmospheric composition as a function of atmospheric height (Section 2.1) and then develop a

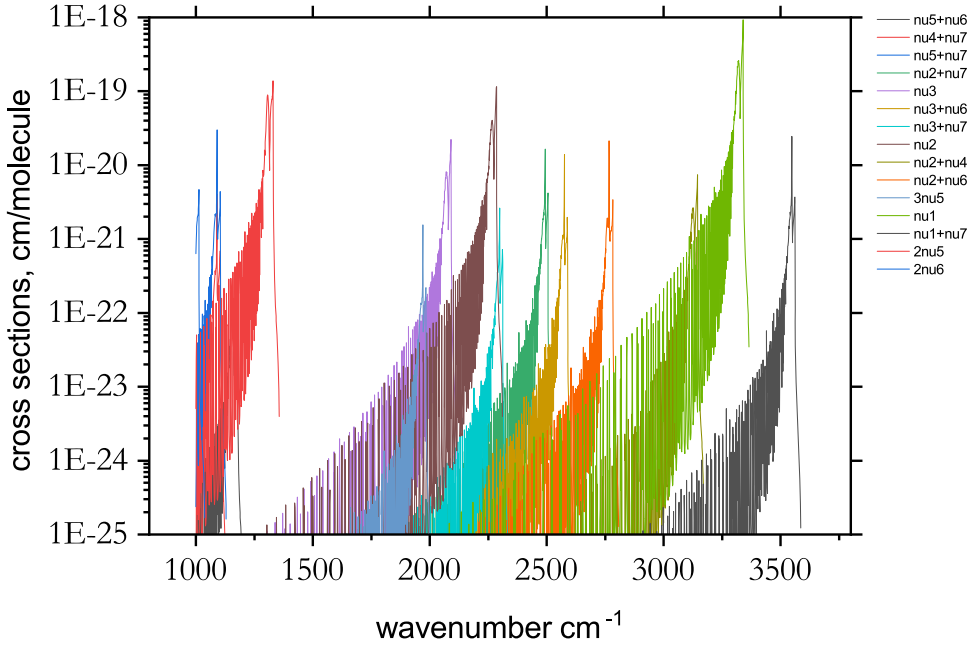

Figure 1. Absorption cross sections of HC_3N at $T = 400$ K: vibrational bands (fundamentals and overtones) used in the spectroscopic model are indicated in the legend.

line list and cross sections for HC_3N (Section 2.2), to model the transmission spectrum of GJ 1132 b (Section 2.3). Finally, we simulate how that spectrum will look if observed by JWST (also Section 2.3).

2.1. Atmospheric Model

Swain et al. (2021) use the ARGO model (Rimmer & Helling 2016) with the STAND2020 chemical network (Rimmer & Rugheimer 2019; Rimmer et al. 2021) and fix surface conditions to predict atmospheric chemical profiles. ARGO is a Lagrangian code that solves the photochemistry-transport equation:

$$\frac{dn_X}{dt} = P_X - L_X n_X - \frac{\partial \Phi_X}{\partial z}, \quad (1)$$

where n_X (cm^{-3}) is the number density of species X, t (s) is time, P_X (cm^{-3} s^{-1}) is the production rate of X, L_X (s^{-1}) is the destruction rate of X, and $\partial\Phi_X/\partial z$ (cm^{-3} s^{-1}) accounts for the vertical transport.

We take the chemical profiles of Swain et al. (2021) as given. This is a self-consistent photochemical model atmosphere, and so the predictions of each of the species are interconnected. Such an atmosphere cannot be rich in carbon dioxide, for example, because carbon dioxide is not a predicted thermochemical or photochemical product in such a reduced atmosphere. We also explore the sensitivity of HC_3N to the concentrations of HCN and CH_4. To do this, we take the $\pm 1\sigma$ errors for the retrieved abundances of HCN and CH_4, from Swain et al. (2021), and apply or model to predict the effect on HC_3N.

2.2. Line List and Cross Sections/k Tables for Cyanoacetylene

There existed no comprehensive IR line list for HC_3N applicable for a broad range of temperatures. The experimental and theoretical information is rather scarce for HC_3N, especially in IR, only for the room temperature (Bénilan et al. 2006; Jolly et al. 2007; Douin et al. 2015; Bizzocchi et al. 2017; Jiang et al. 2021). For this study, we have combined spectroscopic data available for HC_3N in the literature to construct a line list as a best estimate of the opacity of HC_3N in IR. Our synthetic HC_3N line list covers the wavelength range from 2.5 to 10 μm and contains the fundamental ν_1, ν_2, and ν_3 and overtone $2\nu_5$, $2\nu_6$, $3\nu_5$, $\nu_1+\nu_7$, $\nu_2+\nu_4$, $\nu_2+\nu_6$, $\nu_2+\nu_7$, $\nu_3+\nu_6$, $\nu_3+\nu_7$, $\nu_4+\nu_7$, $\nu_4+\nu_7$, $\nu_5+2\nu_7$, and $\nu_5+\nu_6$ bands from this region. Only transitions from the ground vibrational state are included.

We used the program PGOPHER (Western 2017) to generate energies and Einstein coefficients of HC_3N. Spectroscopic constants of $2\nu_6$, $\nu_5+\nu_7$, $\nu_6+\nu_7$, $\nu_6+2\nu_7$, ν_1, ν_2, ν_3, $\nu_1+\nu_7$, $\nu_2+\nu_7$, and $\nu_3+\nu_7$ were taken from the high-resolution IR studies by Bizzocchi et al. (2017) and Jiang et al. (2021). Other states of HC_3N from this IR region have not been characterized experimentally. Their spectroscopic constants were estimated using the constants of the same symmetry and were adjusted to visually agree with the IR spectrum from Bénilan et al. (2006). The corresponding transition-dipole moments were extracted from the ab initio work by Dargelos & Pouchan (2020) computed at the high level of theory CCSD(T)-F12.

A set of temperature-dependent cross sections and k tables were generated using a combination of the program ExoCross (Yurchenko et al. 2018) and the Python library `Exo_k` (Leconte 2020) on the corresponding grids used in PetitRADTRANS (Mollière et al. 2019). Figure 1 illustrates the vibrational bands used to generate the line list for HC_3N.

2.3. Predicted Transmission Spectra

From the atmospheric model, planetary physical parameters, and line opacities of different molecules, the synthetic transmission spectrum was modeled using "PetitRADTRANS"[7] (Mollière et al. 2019) both for a clear and cloudy atmosphere. The atmosphere was considered to be a composition of HC_3N, HCN, CH_4, C_2H_2, CO, CO_2, H_2O, N_2O, and NH_3. Rayleigh scattering from H_2, He, and N_2 was considered, while collision-induced absorption (CIA) opacities for H_2–H_2

[7] https://petitradtrans.readthedocs.io/en/latest/

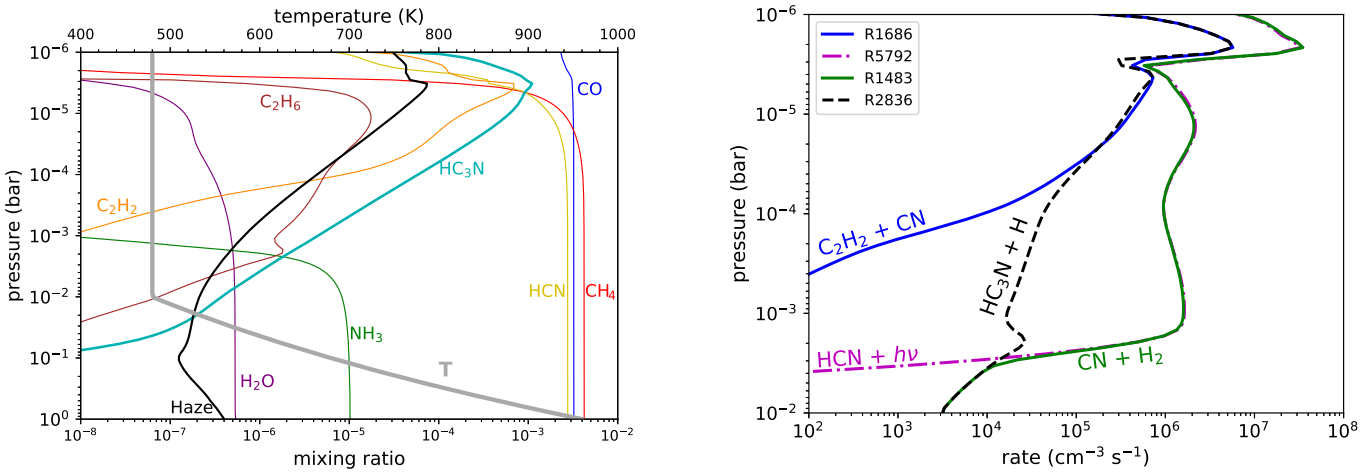

Figure 2. Left: chemical profiles for GJ 1132 b, as mixing ratios as a function of atmospheric pressure (bar), highlighting HC_3N. Taken from Swain et al. (2021, their Figure 11), with permission. Right: rates, in units of cm^{-3} s^{-1}, for critical reactions for the formation and destruction of HC_3N and its precursors, as a function of atmospheric pressure (bar).

and H_2–He were included. A correlated-k approximation mode was used, which resulted in a spectrum of spectral resolution $\lambda/\Delta\lambda = 1000$. To model a cloudy atmosphere, a gray cloud deck was considered at 0.01 bar, which added an opaque cloud deck to the absorption opacity at the given pressure.

To study and analyze the detectability of molecular absorption features in the spectrum from JWST both for a clear and cloudy atmosphere, a noise simulator PandExo (Batalha et al. 2017) package was used. Following the details of modeling as mentioned in Zilinskas et al. (2020), NIRCam grisms in the F322W2 (2.4–4 μm) and F444W (4–5 μm) modes and the MIRI LRS instrument in Slitless mode (5–12 μm) were used to imitate the spectrum. Constant noise levels of 30 ppm for NIRCam and 50 ppm for MIRI LRS were taken with a saturation limit of 80% of full well capacity.

3. Results

Here we present our results for the HC_3N chemistry in the atmosphere of GJ 1132 b, the model transmission spectrum for GJ 1132 b, and the synthetic JWST spectra.

The model atmosphere of GJ 1132 b is sufficient to explain the observations from Swain et al. (2021), which involves a surface chemistry set by degassing primarily of H_2, He, N_2, HCN, CH_4, and CO. Chemical profiles are shown in Figure 2.

A major photochemical product of CH_4 is ethane (C_2H_6), which is then dehydrogenated to acetylene (C_2H_2), which at the high temperatures of the atmosphere of GJ 1132 b can react directly with the photodissociation product of HCN to form HC_3N. The total reaction proceeds as follows:

$$\begin{aligned}
&\mathrm{HCN} + h\nu \rightarrow \mathrm{CN} + \mathrm{H}, && \text{R5792};\\
&2(\mathrm{CH_4} + \mathrm{H} \rightarrow \mathrm{CH_3} + \mathrm{H_2}), && \text{R1520};\\
&\mathrm{CH_3} + \mathrm{CH_3} + \mathrm{M} \rightarrow \mathrm{C_2H_6} + \mathrm{M}, && \text{R143};\\
&\mathrm{C_2H_6} + \mathrm{H} \rightarrow \mathrm{C_2H_5} + \mathrm{H_2}, && \text{R1549};\\
&\mathrm{C_2H_5} + \mathrm{H} \rightarrow \mathrm{C_2H_4} + \mathrm{H_2}, && \text{R1538};\\
&\mathrm{C_2H_4} + h\nu \rightarrow \mathrm{C_2H_2} + \mathrm{H} + \mathrm{H}, && \text{R5841};\\
&\mathrm{CN} + \mathrm{C_2H_2} \rightarrow \mathrm{HC_3}N + \mathrm{H}, && \text{R1686};\\
&\overline{\qquad\qquad\qquad\qquad}\\
&\mathrm{HCN} + 2\mathrm{CH_4} \rightarrow \mathrm{HC_3N} + 4\mathrm{H_2}.
\end{aligned} \tag{2}$$

Cyanoacetylene is destroyed by the reaction with H (R2386 the reverse of R1686), and this simply restores the cyano radical (CN) and acetylene. This reaction has a barrier of ≈9500 K, and this will be important for the steep temperature sensitivity of upper atmospheric cyanoacetylene, as discussed below. The dominant reaction destroying CN is R1483:

$$\mathrm{CN} + \mathrm{H_2} \rightarrow \mathrm{HCN} + \mathrm{H}, \tag{3}$$

which has a barrier of 2370 K. The acetylene undergoes hydrogenation back to C_2H_5, which then reacts with a hydrogen atom and breaks apart into two CH_3 radicals. At low temperatures, these would recombine to form ethane, but at high temperatures, the CH_3 will react with H_2 to reform CH_4. The significant reactions are shown as functions of atmospheric pressure in Figure 2.

We explore how HC_3N varies as HCN and CH_4 are varied. We vary both HCN and CH_4 over the 1σ retrieved abundances of Swain et al. (2021) and plot the predicted HC_3N profiles in Figure 3. HCN abundance determines the peak of the HC_3N profile, with some influence from CH_4. CH_4 also influences the overall shape of the HC_3N profile.

We also explore how HC_3N varies with temperature and chemical mixing, expressed by varying the eddy diffusion coefficient (K_{zz}, cm^2 s^{-1}). We performed a sensitivity analysis with fixed HCN and CH_4 at 0.5%, varying stratospheric temperature from 300 to 1000 K (with fixed $K_{zz} = 10^7$ cm^2 s^{-1}), and eddy diffusion coefficient from 10^5 to 10^{10} cm^2 s^{-1} (with a fixed stratospheric temperature of 480 K).

We show the predicted transmission spectra in Figure 4 and the JWST simulated observtions in Figure 5, with uncertainties resulting from our sensitivity analyses. As we can see in these figures, the absorption lines corresponding to HC_3N are very narrow, and a reason for that could be its abundance is only in the upper atmosphere, i.e., at low pressure, where pressure broadening is minimal. To resolve these narrow absorption lines, we had need high spectral resolution. At a spectral resolution of 100 and one transit, the peaks of HC_3N at around 4.5 and 9 μm nevertheless seem distinguishable. If we increase the number of transits to four, we see only a slight change in the values of error bars at higher wavelength

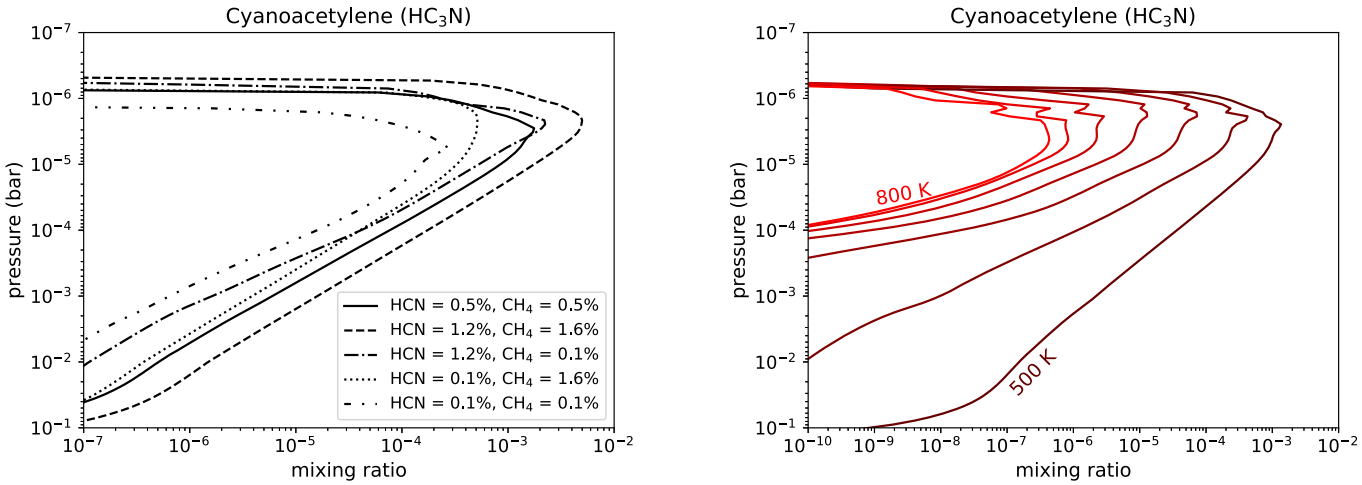

Figure 3. Cyanoacetylene (HC_3N) mixing ratio as a function of atmospheric pressure (bar). Left: predicted for a 10% N_2, 90% H_2 atmosphere with the retrieved abundances and errors of Swain et al. (2021): $0.5\% + 0.7\% - 0.4\%$ HCN and $0.5\% + 1.1\% - 0.4\%$ CH_4. C_2H_2 is set to 100 ppm. Right: predicted for 10% N_2, 90% H_2, 0.5% HCN, and CH_4, as a function of stratospheric temperature. Colors proceed from dark red, 500 K, to light red, 800 K, in 50 K steps.

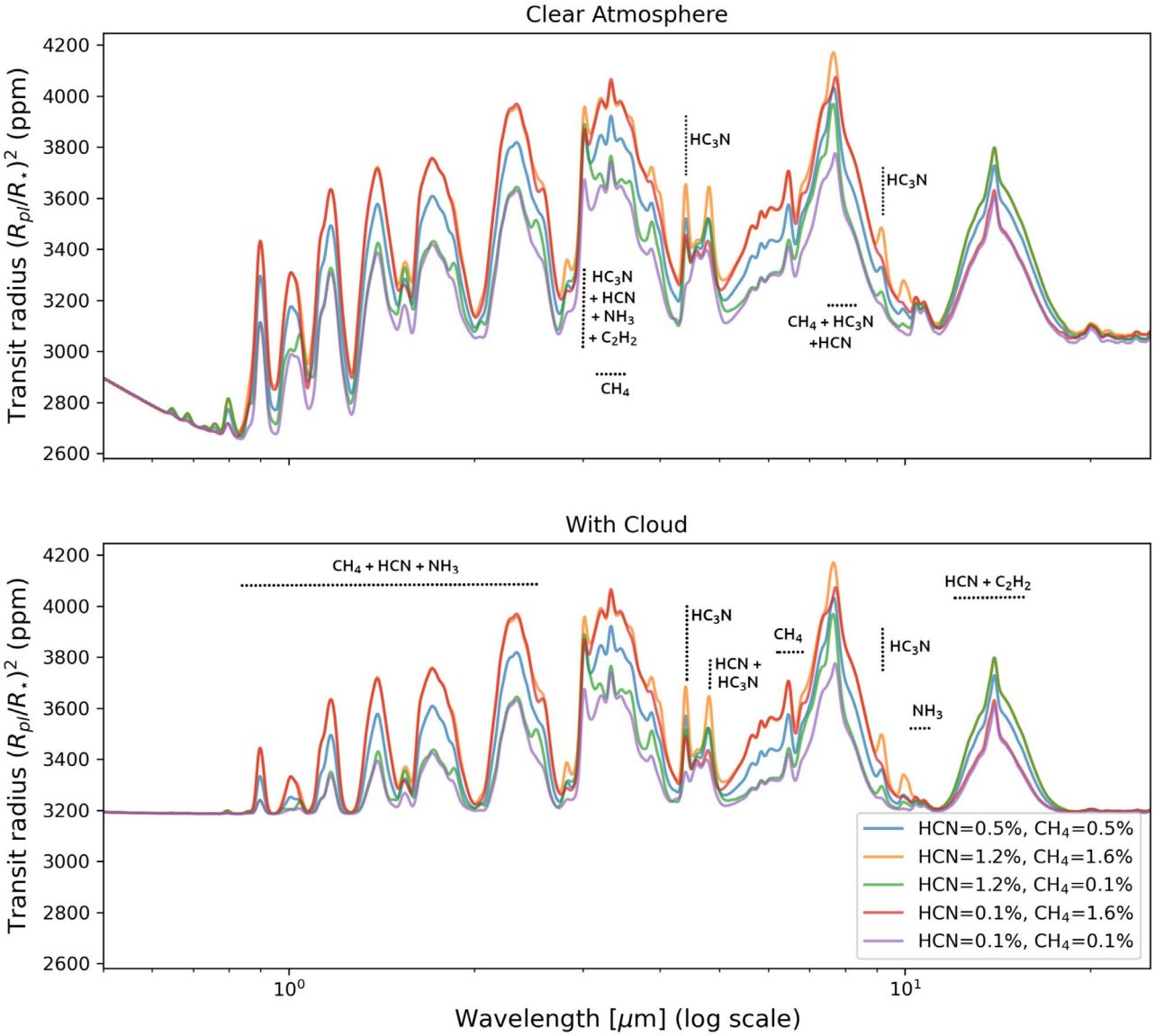

Figure 4. Simulated transmission spectrum of GJ1132b using the ARGO photochemistry model and the PETITRADTRANS radiative transfer package for different HCN and CH_4 compositions. The cloud was modeled according to the power-law function, considering a gray cloud at $P = 0.01$ bar. The spectrum is shown at a resolution of 100, which was generated by convolving the high-resolution data ($R = 1000$) with a Gaussian kernel of standard deviation = 8.4506.

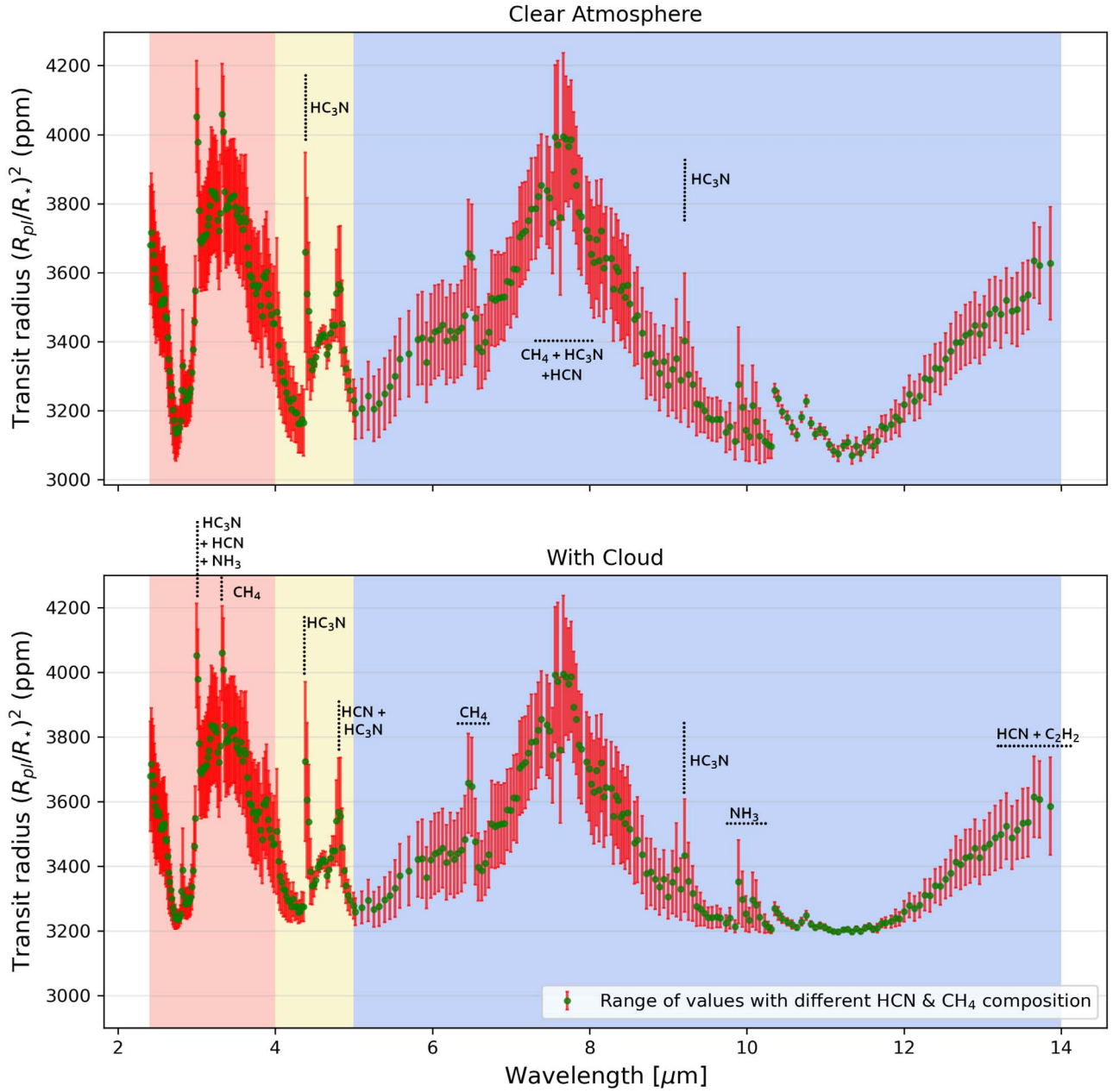

Figure 5. The range of values in the JWST simulated observation using PandExo for different HCN and CH_4 compositions, after one transit and with a resolution of 100. The cloud was modeled according to the power-law function, considering a gray cloud at $P = 0.01$ bar. The three colors denote the three JWST modes and instruments used, which were NIRCam grism F322W2, NIRCam grism F444W, and MIRI LRS.

regions, but it does not noticeably affect the error bars near HC_3N features. Even after considering cloudy atmosphere, an HC_3N feature is fairly detectable at around 9 μm when we have high HCN and CH_4. In all cases except when HCN and CH_4 both are low, the 4.5 μm HC_3N line is readily detectable. The absorption features of other major molecules, viz. CH_4 and HCN, are very prominent and have broad absorption lines in the generated spectrum, which aligns very well with their high abundance of those molecules, specifically in the higher-pressure region as shown in the plot of pressure versus mixing ratio of species. At least one of the HC_3N features is detectable for a stratospheric temperature $\lesssim$600 K, as shown in Figure 3, and an eddy diffusion coefficient between 10^6 cm^2 s^{-1} $\lesssim K_{zz} \lesssim$ 10^9 cm^2 s^{-1}. If we decrease the spectral resolution to 50, we can still distinguish the HC_3N feature at 4.5 μm for most of the models (except the model with 0.1% HCN and 0.1% CH_4), whereas the HC_3N feature at 9 μm remains undetectable for most of the models (except the model with 1.2% HCN and 1.6% CH_4). Thus, the spectral resolution of 100 is required to detect both the HC_3N features simultaneously.

We see in Figure 3 that the mixing ratio of HC_3N is strongly dependent on stratospheric temperature, and drops below 1 ppm in the upper atmosphere when $T \gtrsim 700$ K. The relative strength of these lines and others in the upper atmosphere is also affected by the temperature, and at high temperatures, $\gtrsim$600 K, HC_3N will be very difficult to detect. Above $\sim$700 K, no observable features remain.

This temperature sensitivity can be explained by R2386 (discussed above):

$$HC_3N + H \rightarrow C_2H_2 + CN. \quad (4)$$

The rate constant for this reaction between 450 and 800 K is effectively $2.5 \times 10^{-10}\,cm^3\,s^{-1}\exp(-9500\,K/T)$, and production does not change by more than a factor of a few over this range, and so balancing production and destruction at $\sim 10^{-5}$ bar, one finds an analytic estimate of the peak mixing ratio of cyanoacetylene ($x(HC_3N)$):

$$x(HC_3N) \approx 4 \times 10^{-12}\, e^{9500/T}, \quad 450\,K \leqslant T \leqslant 800\,K. \quad (5)$$

This explains the chemical mechanism for the loss of cyanoacetylene at higher stratospheric temperatures.

4. Discussion and Conclusion

In this Letter, we show that, if GJ 1132 b has observable amounts of CH_4 and HCN in its atmosphere, as reported by Swain et al. (2021), we predict it will have up to 0.5% of HC_3N in its upper atmosphere due to photochemistry. Applying radiative transfer and accounting for the properties of JWST, we predict that cyanoacetylene (HC_3N) will be observable by JWST, given what we currently know about the molecule.

There is some uncertainty about the HC_3N line list (limited coverage of vibrational bands), but these uncertainties are small compared to the uncertain composition of the atmosphere, with retrieved HCN and CH_4 abundances spanning more than an order of magnitude and the predicted HC_3N abundances spanning a factor of 30. These uncertainties were incorporated into the spectra, and we found that spectral features of the molecules remain detectable at $\gtrsim$0.1% mixing ratios of HCN and CH_4, the low end of the 1σ error bars for these species retrieved abundances. More work will be needed, both experimental and theoretical, in order to make any strong claim about the shape and strength of HC_3N features for temperatures $\gg$500 K, where otherwise energetically prohibitive and therefore yet unknown bands will be accessed, and the spectrum of HC_3N could be significantly different. As we have found, however, HC_3N abundance decreases to below detectable levels (concentrations of 10–100 ppm) at temperatures $\gtrsim$600 K, at least in the reducing rocky planet atmosphere we explore. For our bulk atmospheric composition, HC_3N may not be detectable at such high stratospheric temperatures because it will not survive in those temperatures; see Equation (5). We found that HC_3N concentrations were far less sensitive to the eddy diffusion coefficient, remaining detectable between values of 10^6 and 10^{10} cm^2 s^{-1}.

Even if GJ 1132 b does not have HCN, there are many planets, including, plausibly, many rocky planets that may host hydrogen-rich atmospheres rich in HCN (Tsiaras et al. 2016). Super-Earths also may host reduced atmospheres because of quenched mantle differentiation (Lichtenberg 2021). For reduced atmospheres of rocky planets, HC_3N is an important opacity source that retrieval models should take into account.

By itself, HC_3N cannot be uniquely identified by observing one or two spectral features. Rather, it will be the presence in the context of a hydrogen-rich exoplanet atmosphere. The probability that HC_3N is an explanation for a given spectral feature must be assessed in the context of other molecular constituents as indicated by the full transmission spectra, such as H_2 (inferred from the scale height), CH_4, and HCN. In this context, HC_3N would be a further indicator of the presence of HCN, and a probe into prebiotically relevant mechanisms taking place on uninhabitable planets. This may give a window into the time when our planet was hot and hydrogen-rich (Genda et al. 2017), forming molecules that later may have been essential to the origins of life.

The authors thank Mark Swain for helpful comments on the paper. P.B.R. thanks the Simons Foundation for funding (SCOL awards 599634). S.Y.'s work was supported by the STFC Project ST/R000476/1 and by the European Research Council (ERC) under the European Union's Horizon 2020 research and innovation programme through Advance grant No. 883830. S.W. was supported through the STFC UCL CDT in Data Intensive Science (grant No. ST/P006736/1).

Software: ARGO (Rimmer & Helling 2016), PETITRADTRANS (Mollière et al. 2019), PANDEXO (Batalha et al. 2017), `Exo_k` (Leconte 2020), EXOCROSS (Yurchenko et al. 2018).

ORCID iDs

Paul B. Rimmer https://orcid.org/0000-0002-7180-081X
Liton Majumdar https://orcid.org/0000-0001-7031-8039
Akshay Priyadarshi https://orcid.org/0000-0003-1143-0877
S. N. Yurchenko https://orcid.org/0000-0001-9286-9501

References

Batalha, N. E., Mandell, A., Pontoppidan, K., et al. 2017, PASP, 129, 064501
Becker, S., Feldmann, J., Wiedemann, S., et al. 2019, Sci, 366, 76
Bénilan, Y., Jolly, A., Raulin, F., & Guillemin, J.-C. 2006, P&SS, 54, 635
Bézard, B., Marten, A., & Paubert, G. 1992, BAAS, 24, 953
Bizzocchi, L., Tamassia, F., Laas, J., et al. 2017, ApJS, 233, 11
Dargelos, A., & Pouchan, C. 2020, CPL, 754, 137746
Diamond-Lowe, H., Berta-Thompson, Z., Charbonneau, D., & Kempton, E. M. R. 2018, AJ, 156, 42
Douin, S., Gronowski, M., Lamarre, N., et al. 2015, JMoSp, 119, 9494
Ferris, J. P., Sanchez, R. A., & Orgel, L. E. 1968, J. Mol. Biol., 33, 693
Genda, H., Brasser, R., & Mojzsis, S. J. 2017, E&PSL, 480, 25
Jiang, N., Melosso, M., Tamassia, F., et al. 2021, FrASS, 8, 29
Jolly, A., Benilan, Y., & Fayt, A. 2007, JMoSp, 242, 46
Khanna, R. K. 2005, Icar, 178, 165
Leconte, J. 2020, A&A, 645, A20
Libby-Roberts, J. E., Berta-Thompson, Z. K., Diamond-Lowe, H., et al. 2021, arXiv:2105.10487
Lichtenberg, T. 2021, ApJL, 914, L4
Miller, S. L. 1953, Sci, 117, 528
Mollière, P., Wardenier, J., van Boekel, R., et al. 2019, A&A, 627, A67
Mugnai, L. V., Modirrousta-Galian, D., Edwards, B., et al. 2021, AJ, 161, 284
Orgel, L. E. 2002, OLEB, 32, 279
Powner, M. W., Gerland, B., & Sutherland, J. D. 2009, Natur, 459, 239
Rimmer, P. B., & Helling, C. 2016, ApJS, 224, 9
Rimmer, P. B., Jordan, S., Constantinou, T., et al. 2021, PSJ, 2, 133
Rimmer, P. B., & Rugheimer, S. 2019, Icar, 329, 124
Sanchez, R. A., Ferris, J. P., & Orgel, L. E. 1966, Sci, 154, 784
Schaefer, L., Wordsworth, R. D., Berta-Thompson, Z., & Sasselov, D. 2016, ApJ, 829, 63
Southworth, J., Mancini, L., Madhusudhan, N., et al. 2017, AJ, 153, 191
Swain, M. R., Estrela, R., Roudier, G. M., et al. 2021, AJ, 161, 213
Thelen, A. E., Nixon, C. A., Chanover, N. J., et al. 2019, Icar, 319, 417
Tsiaras, A., Rocchetto, M., Waldmann, I. P., et al. 2016, ApJ, 820, 99
Western, C. M. 2017, JQSRT, 186, 221
Yurchenko, S. N., Al-Refaie, A. F., & Tennyson, J. 2018, A&A, 614, A131
Zilinskas, M., Miguel, Y., Mollière, P., & Tsai, S.-M. 2020, MNRAS, 494, 1490